Busbars for e-mobility: State-of-the-Art Review and a New Joining by Forming Technology

F. V. Sampaio, Rui ; Zwicker, Maximilian F. R.; Pragana, João P. M. ; M. F. Bragança , Ivo ; Silva, Carlos M.A. ; Nielsen, Chris V.; Martins, Paulo A. F.

Published in:
Mechanical and Industrial Engineering. Materials Forming, Machining and Tribology

Link to article, DOI:
10.1007/978-3-030-90487-6_4

Publication date:
2022

Document Version
Peer reviewed version

1. Busbars for e-mobility: State-of-the-art review and a new joining by forming technology

Rui F.V. Sampaio[a], Maximilian F.R. Zwicker[b], João P.M. Pragana[a], Ivo M.F. Bragança[c], Carlos M.A. Silva[a], Chris V. Nielsen[b] and Paulo A.F. Martins[a]

[a]IDMEC, Instituto Superior Técnico, Technical University of Lisbon, Av. Rovisco Pais, 1049-001 Lisboa, Portugal.

[b]Department of Mechanical Engineering, Technical University of Denmark, Produktionstorvet, 2800 Kgs. Lyngby

[c]CIMOSM, Instituto Superior de Engenharia de Lisboa, Instituto Politécnico de Lisboa, Portugal.

E-mails: rui.f.sampaio@tecnico.ulisboa.pt, mfrz@mek.dtu.dk, joao.pragana@tecnico.ulisboa.pt, ibragança@dem.isel.ipl.pt, carlos.alves.silva@tecnico.ulisboa.pt, cvni@mek.dtu.dk, pmartins@tecnico.ulisboa.pt

Abstract

The changes in the automotive market and their effects on industry are nowadays hot topics in metal forming seminars and conferences around the world. The rise in the number of electric vehicles will inevitably lead to a decrease in the demand of components for combustion engines and power drive trains. Typical forming components such as pistons, connecting rods, valves, camshafts, crankshafts, multi-speed gear boxes and others that exist in diesel or petrol vehicles, will no longer be required.

However, the lightweight construction requirements for the body-in-white of electric vehicles, the production of components for asynchronous motors and the fabrication of battery components, namely busbars, are bringing new challenges and opportunities for the metal forming industry. This chapter is focused on busbars, which are metallic strips or sheets that are utilized to distribute electric power to multiple equipment such as the electric motor, the electric power steering unit, and the AC/DC converters. In particular, the chapter addresses the challenge of replacing copper busbars by hybrid busbars made from copper and aluminium, due to the expected savings in weight and cost.

For this purpose, the authors discuss the challenge of connecting copper to aluminium in hybrid busbars by means of existing joining technologies and introduce a new joining by forming process aimed at connecting hybrid busbars at room temperature without giving rise to material protrusions above and below the sheet surfaces. The effectiveness of the new process is compared against fastening by measuring the electric resistivities in both types of hybrid busbar joints. Finite element analysis gives support to the presentation and proves to be suitable for the electro-thermo-mechanical analysis of busbar connections.

1.1 Introduction

E-mobility, or electromobility, is defined as a road transport system in which vehicles are moved by electricity. It is believed to play a key role in the increase of flexibility in transportation because electric vehicles may use different types of energy sources, as electricity can be obtained from nuclear power, fossil fuels, or renewable resources. This gives electric vehicles some advantages over internal combustion engine (ICE) vehicles while contributing to lower CO_2 emissions, especially if electricity is produced by nuclear power or renewable sources.

Electric vehicles appeared at the end of the 19th century and the first commercially available electric vehicle was developed in 1897 by the *Electric Carriage and Wagon Company* [1]. Although technological development is usually motivated by costumer preference, this has not been the case in electromobility. In fact, costumers are mostly pleased with their ICE vehicles, and fossil fuels are not expensive enough to stimulate a move into electric vehicles. The consistent underpricing of fossil fuels (Fig. 1.1) is also an obstacle to the transition to electromobility [2].

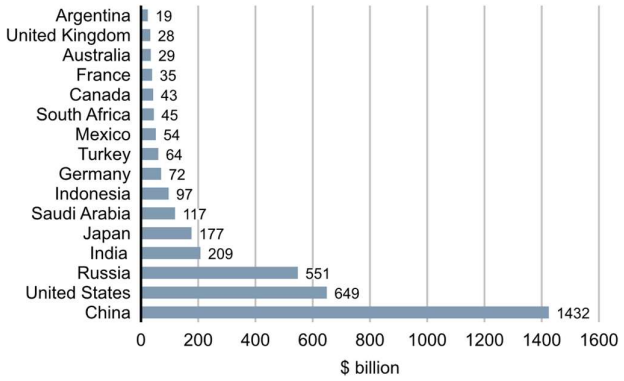

Fig. 1.1 *Underpricing of fossil fuels in the G20 economies in 2015 (adapted from [2]).*

However, electromobility is nowadays a route for automakers to be ahead of their competitors in terms of green thinking and environmental compliance. Lower taxes on electric cars are in many countries stimulating consumers to move from ICE to electric vehicles.

It is worth noticing that the importance of hybrid busbars is not limited to electric vehicles because alternative mobility solutions based on hydrogen is heavily dependent on the installation of water electrolysis plants [3] in which electricity running through busbar systems will be used to decompose water into oxygen and hydrogen [4]. Hydrogen produced in water electrolysis plants can also contribute to zero carbon emission objectives in e-mobility if the electricity is produced from renewable sources.

1.1.1 Busbars and busbar systems

The distribution of electric power is carried out by wires, cables, and busbars. Busbars are generally preferred in low-voltage (LV—up to 1 kV) systems with high electric currents because of their advantages regarding ease of installation and maintenance (flexibility), safety, cost, and limitations in space. In fact, the utilization of a high number of cables in parallel for high current applications is not a good solution due to difficulties in installation and maintenance and to troubles in diagnosing and locating problems in the distribution of electric power.

Especially in power plants, six different types of busbar systems can be identified (Fig. 1.2): (i) non-segregated busbars, (ii) segregated busbars, (iii) isolated phase busbars, (iv) rising mains (vertical busbar systems), (v) overhead busbars (horizontal busbar systems), and (vi) non-conventional busbars (like sandwich or gas insulated) [5]. Some of these (e.g., isolated phase busbars) are applied in electric vehicles while others are included for broadening the presentation.

In non-segregated systems (Fig. 1.2a), the busbars (corresponding to the different phases) are stored in a single metallic enclosure, where insulating supports maintain a certain distance between the busbars and to the enclosure. There are no barriers between them. These systems are simple, economic and are the most widely used in LV systems up to electric currents of approximately 6 kA.

In segregated systems (Fig. 1.2b), the busbars are also stored in a single enclosure, but there is an additional metallic barrier between each busbar. These barriers are constructed from the same material as the enclosure (usually aluminum) and provide magnetic shielding, isolating each busbar from the others and protecting the phases against short-circuits. They behave somewhat like a Faraday cage, so that parasitic currents are drawn to the aluminum barrier rather than to the other phases. Although being preferred for high voltage (HV—from 35 to 230kV) rather than for LV, this type of busbar system is used for high electric currents (3-6 kA) on all voltage systems.

In isolated phase systems (Fig. 1.2c), each busbar is kept in an individual non-magnetic metallic container to prevent phase-to-phase faults, eliminate proximity effects (e.g., heating), facilitate installation and maintenance, and protect operators from high voltages across the enclosure and metallic structures that arise from parasitic electro-magnetic currents. Isolated phase systems are utilized for extremely large electric currents (above 10 kA) in HV systems.

Rising main systems (Fig. 1.2d) are vertically running busbar systems used for power distribution in multistorey high-rise buildings, allowing for power supply to the multiple floors. This type of system usually operates with very low electric currents and, therefore, is not the best choice from an economical point of view.

Overhead busbar systems (Fig. 1.2e) run horizontally, usually below ceilings, and are used to distribute power through a single floor. Large rooms with machine tools may largely benefit from overhead busbar systems, as cables become unwieldy.

Non-conventional systems (Fig. 1.2f) try to replicate the compactness advantages of cables in busbars by using proper insulation techniques, in which heat transfer occurs by conduction rather than convection through air, as in case of conventional systems (Figs 1.2a-1.2e). In fact, the poor dissipation of heat by natural air convection is one of the reasons why conventional busbar systems rely on the use of busbars and enclosures with large cross-sections.

Thus, non-conventional systems are not only more compact, but also more energy-efficient for both LV and HV applications. In sandwich busbars, insulation is achieved by means of epoxy or thin films of polyester. By also coating the inside of the enclosure, busbars can be placed touching each other and the enclosure.

Gas insulated busbars allow electric power distribution in HV systems with electric currents up to 8 kA. They are used in gas insulated switchgear substations to interconnect the switchgear with the transformer. These systems are modularly constructed and the flanged geometry at the end of every segment allows for rapid and easy installation and replacement [6].

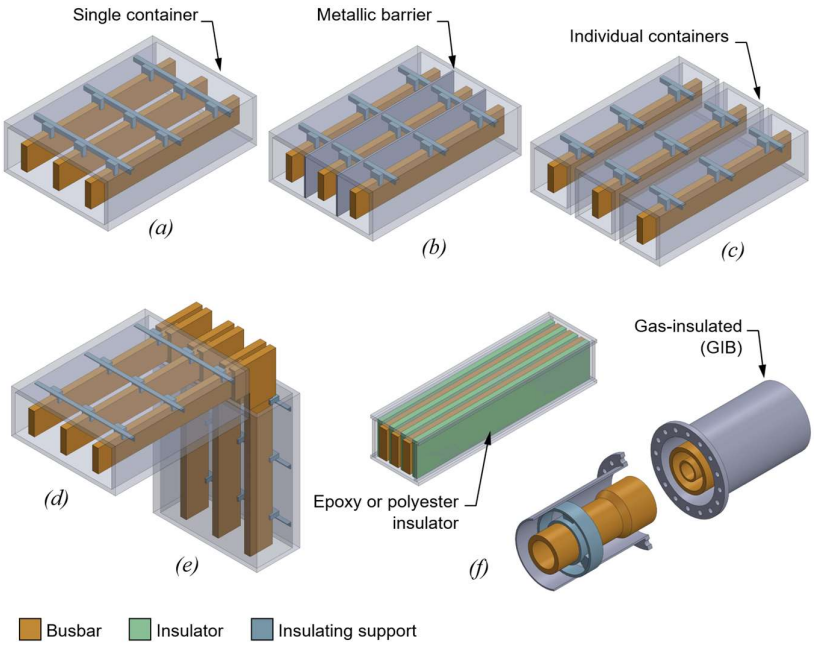

Fig. 1.2 *Different types of busbar systems where each phase has only one busbar. (a) non-segregated, (b) segregated, (c) isolated phase, (d) overhead, (e) rising mains, and (f) non-conventional.*

Busbars can have various cross-sectional shapes (Fig. 1.3): (i) circular, (ii) tubular, (iii) rectangular, and (iv) complex geometries such as the U or H-shapes [7] and the tunnel shape [8]. Guidelines for estimating the heat dissipation by natural and forced convection, and by radiation in each cross-section shape of Fig. 1.3 are provided in the above-mentioned references [7, 8].

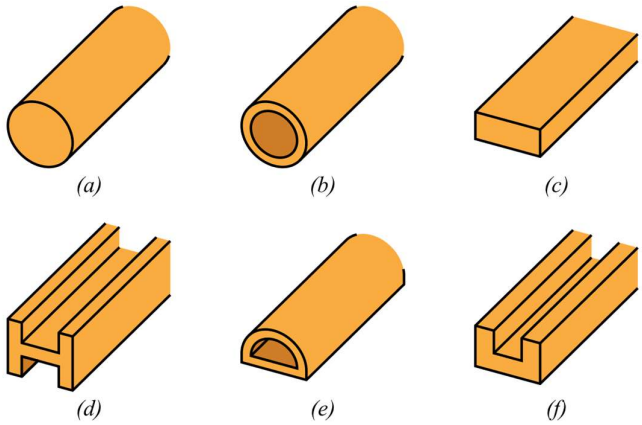

Fig. 1.3 *Schematic representation of several busbar geometries: (a) circular, (b) tubular, (c) rectangular, (d) H-shaped, (e) U-shaped, and (f) tunnel-shaped.*

Busbars are preferentially made of copper due to its high electric conductivity. However, because aluminium is a good electrical conductor that is both lighter and cheaper than copper, there is a growing interest in utilizing aluminium busbars. However, the switch from copper to aluminium comes at the cost of diminishing the current carrying capacity and increasing the overall impedance of the busbars.

This means that the cross section of the aluminium busbars must be increased to obtain an electric power performance like that of copper.

The greater hardness, lower coefficient of linear thermal expansion and higher melting point of copper are also advantageous because the busbars can be made more resistant to mechanical damage during installation and service, and less sensitive to thermal damage caused by localized hot spots or possible flashovers during operation.

Still, both copper and aluminium have high affinity to oxygen and therefore, naturally create oxide films in contact with air. While the copper oxide film is still conductive, the aluminium oxides have insulating properties, which may cause long term problems in the distribution of electric power [7].

One solution to combine the technical advantages of copper with the lightweight and economic advantages of aluminium is by using copper-clad aluminium (CCA). Copper-clad aluminium was developed for wires in the late 1960's [9] and later applied to busbars [10]. CCA is named as Cuponal when used in busbars and consists of a metal composite bar in which the core is made of aluminium and the skin is made of copper.

When compared to copper, CCA has a lower density and cost, while maintaining excellent electric and thermal conduction properties and giving rise to oxide layers that are irrelevant for the electric conductivity in busbar systems. Table 1.1 presents a comparison of physical, mechanical, and economic data for copper, aluminium and CCA/Cuponal.

Table 1.1 *Physical, electrical, thermal, mechanical, and economic data for copper, aluminium, and CCA/Cuponal.*

	Copper[a]	**Aluminium**[b]	**CCA/*Cuponal***
Typical grades used in busbars	C11XXX	AA 1XXX AA 6XXX	—
Density (kg/m^3)	~8900	2680–2920	Slightly higher than aluminium
Melting point (ºC)	~1080	~660	—
Electrical resistivity (μΩ·m)	0.0168–0.0172	0.0267–0.047	Slightly lower than aluminium
Oxide's electrical resistance	Negligible for busbar applications	High	Similar to copper
Thermal conductivity (W/(m·K))	385–388	167–234	Slightly higher than aluminium
Coefficient of thermal expansion (1/K)	~17 x 10^{-6}	~24 x 10^{-6}	—
Yield strength (MPa)	69–365	28–324	—
Ultimate tensile strength (MPa)	220–455	51–414	—
Elongation (%)	4–50	4–19	—
Hardness (HB)	< 112	< 95	—
Machinability index (%)[c]	60 %	>125 %	—
Cost	Almost 4 times higher than aluminium	—	Lower than copper, but higher than aluminium

[a]Values for C11000 series [11].
[b]Values for AA 1000 and AA 6000 series [12].
[c]Values in % of B1112 base steel [13].

Another solution to combine the technical advantages of copper with the lightweight and economic advantages of aluminium is by using hybrid busbars, in which the thinner and costlier parts made of copper are only used in specific key locations. In current state-of-technology, this requires connecting copper to aluminium by

means of overlapped joints produced by conventional joining processes such as welding and fastening, which is not always possible or effective to achieve.

Moreover, the electrical resistance of the overlapped joints increases with the reduction of the overlap length, due to streamline distortion of the electric current distribution, and temperature also increases due to a smaller area available for heat dissipation [14].

1.1.2 Batteries and electric power distribution in e-mobility

Besides the energy applications, busbars are essential components of battery packs for electrified vehicles. Electric, plug-in hybrid-electric, and hybrid-electric-vehicle's battery packs are modularly designed and consist of several cells. Most electric vehicles (EVs) and plug-in hybrid-electric vehicles (PHEVs) use lithium-ion battery cells, while most hybrid-electric vehicles (HEVs) use nickel-metal hydride battery cells [15].

The battery cells can be cylindrical, prismatic, or pouch-shaped (Fig. 1.4) and are interconnected (either in series or in parallel) by means of busbars joined to the cell terminals to create battery modules (Fig. 1.5) [16]. These busbars will be referred to as primary busbars. The battery modules are then connected to each other in series by busbars to create the battery pack. These busbars are then referred to as secondary busbars.

While parallel connections are deployed to enhance the module capacity, series connections ensure the overall voltage, which ranges between 100-200 V for HEVs and 400-800 V for EVs [17].

Cylindrical cell	Prismatic cell	Pouch cell
	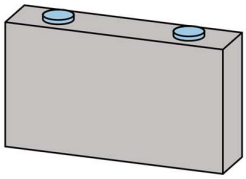	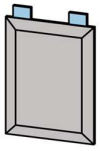
Small size Hard casing Low individual cell capacity Built-in safety features Comparably cheap	Hard casing Large size High individual cell capacity	Soft casing Large size High individual cell capacity Geometrical deformation during charging and recharging

Fig. 1.4 *Different types of battery cells and their main characteristics (adapted from [16]).*

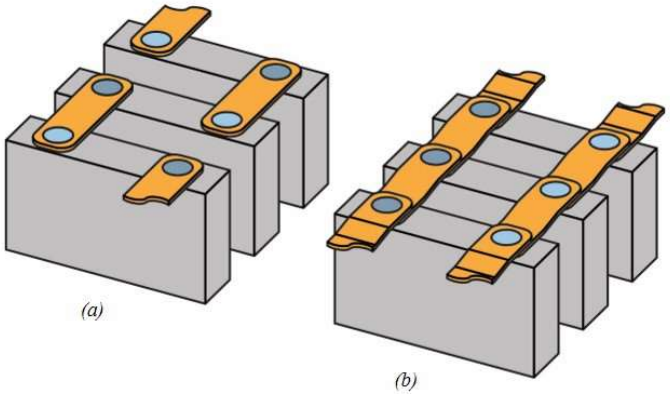

Fig. 1.5 *Interconnection of prismatic battery cells in: (a) series connection and (b) parallel connection.*

Primary busbars may have different dimensions, designs, and material choice depending on the battery cell type as exemplified in Fig 1.6. Typical busbar plates are shown in Fig. 1.6a and 1.6b. They are used for the parallel interconnection of cylindrical cells. In the examples, they are joined by wire bonding (Fig. 1.6a) and laser welding (Fig. 1.6b). Pouch cells may be connected by thicker busbars (Fig 1.6c) or U-shaped busbars (Fig 1.6d). Prismatic cells are commonly connected in series, which may be solved by busbars depicted in Fig 1.6e and Fig 1.6f. The thickness of those busbar systems may range from 0.5 mm to 5 mm in some cases. Common materials, characterized by a high electrical conductivity, are among others copper-, aluminium-, nickel-, and nickel-plated steels.

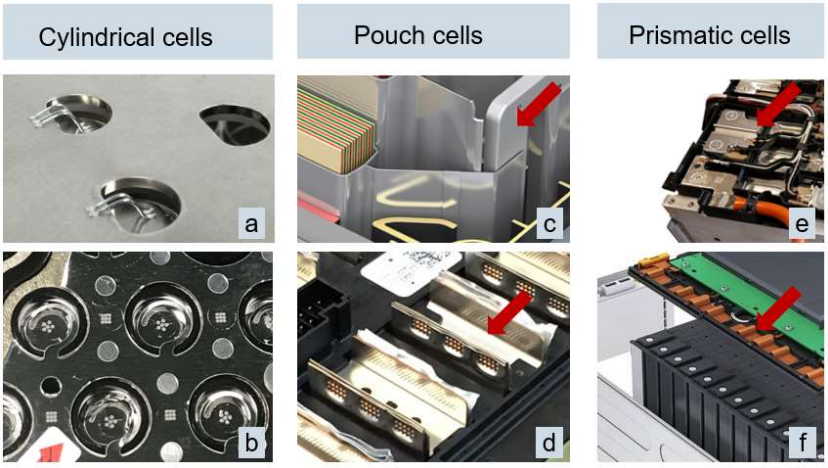

Fig. 1.6 *Different types of primary busbars: connector plates for cylindrical cells (a) (adapted from [18]) and (b) (adapted from [19]); busbars for pouch cells (c) busbar plate (adapted from [20]) and (d) u-shaped busbar (adapted from [21]); busbars for prismatic cells (e) (adapted from [22]) and (f) (adapted from [23]).*

Secondary busbars are often realized by isolated phase busbar systems (Fig. 1.2c). Here, each busbar represents a phase, and the enclosure is the insulating coating. Secondary busbars not only connect, as mentioned, the various battery modules (Fig 1.7) but are also utilized to distribute electrical power from the charging point to the battery pack and from there to multiple pieces of power electronics, e.g., the electric motor or the electric power steering unit.

As shown in Fig. 1.7, the total length of secondary busbars installed in an electric vehicle (depicted in orange colour) represents a large amount of material. This would result in high weight and costs for automakers if busbars were exclusively made of copper. However, this is not the case due to the generalized use of hybrid copper-aluminium busbars in all types of electric vehicles. Hybrid busbars provide efficient, low cost and low weight electric power distribution solutions [24], and its design is generally made in such a way that the thinner and costlier copper strips are only used in specific locations, where high conductivity is necessary (e.g., at the busbar ends).

The resulting modular structure of EV and HEV battery packs must be designed such that it ensures durability and accounts for the protection against crashes or possible mechanical damage. Furthermore, insulation against vibrations and prevention of exothermic reactions accelerated by an increase of temperature (thermal runaways), are essential requirements for battery packs [23].

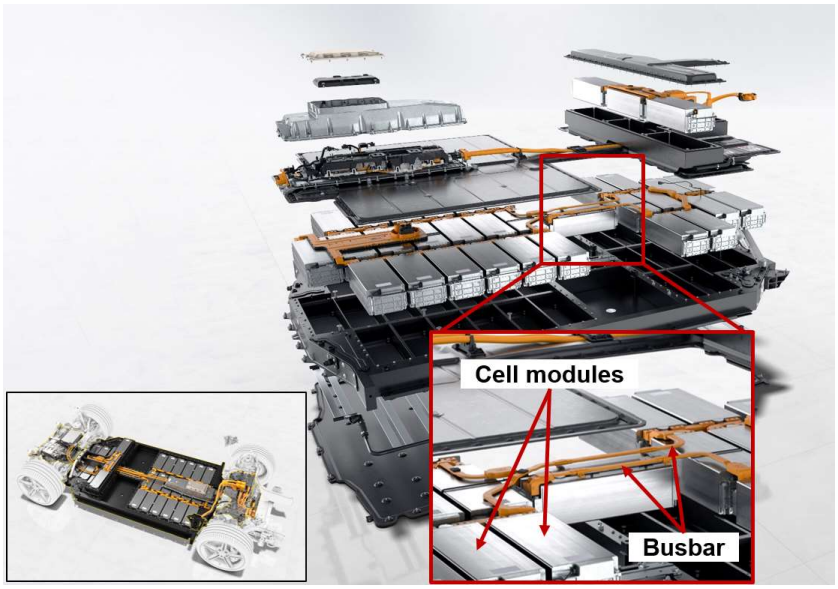

Fig. 1.7 *Representation of the electrical power distribution system in the Porsche Taycan Turbo S (adapted from [25]).*

1.1.3 Joining processes

Traditional requirements for joints and joining technologies are mostly of mechanical nature in combination with requirements due to corrosion and metallurgy. However, when joining busbars, e.g., for automotive or power plant applications, the electrical properties of the joint become also a crucial factor. This interdisciplinary consideration is essential as both aspects are inter-dependent. If a joint is of good mechanical strength but of high electrical resistance, the joint area will heat up due to current flow. This in turn may affect the metallurgical properties of the joint such that the mechanical properties are impaired, which may again affect the electrical and corrosive properties.
Therefore, the main challenges related to joining of busbars to other busbars or cell terminals for automotive and energy applications are the following (cf. [16], where also further details are found):

(a) The joints must be fabricated with low electrical resistance to generally minimize Joule heating of the joint region when primary and secondary busbars are in operation. Additionally, the connection resistance should have the smallest possible scattering range in order to avoid unbalanced charging and discharging of parallel connected cells [26].
(b) The joining technology for primary busbars must have a low heat input to avoid exposing the cells to high temperatures that may harm the battery chemistry [27].
(c) The joints must be fabricated with good mechanical strength and without internal damage of the cells due to application of excessive mechanical loads, including vibrational loads.
(d) The joints must have high resistance to thermal fatigue to guarantee durability and lasting performance.
(e) The joints in busbars made from dissimilar materials (hybrid busbars) must account for the problems related to contact corrosion, micro cracking, and formation of hard and brittle, highly resistive, intermetallic compounds [28].

(f) The joints in busbars made from dissimilar materials must account for the differences in performance arising from the utilization of materials with different thicknesses, electric conductivities, thermal expansions, and coatings [29].

The main joining processes that are nowadays used for joining cell terminals to busbar connectors and for joining busbars are schematically illustrated in Fig. 1.8. These processes belong to the four different groups that are classified in Table 1.2.

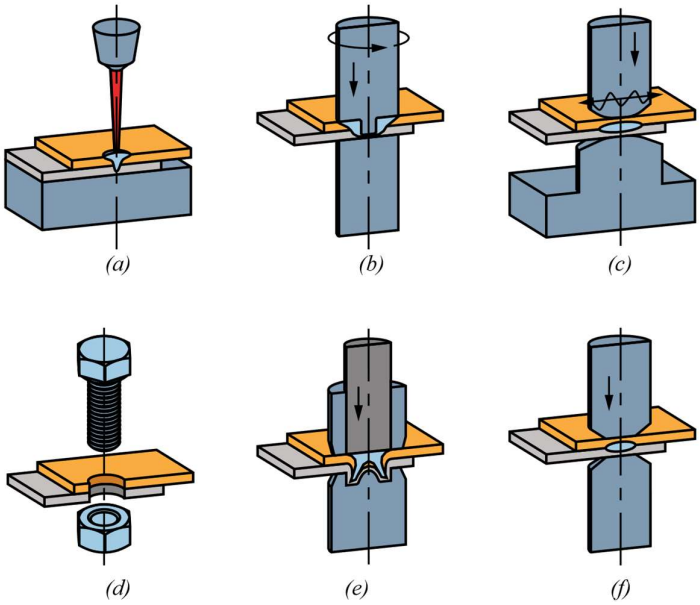

Fig. 1.8 *Schematic representation of the main joining processes that are currently utilized to connect cell terminals to busbars and for joining monolithic and hybrid busbars: (a) laser beam welding, (b) friction stir spot welding, (c) ultrasonic welding, (d) fastening, (e) self-pierce riveting and (f) resistance spot welding.*

Table 1.2 *Classification of the joining processes more utilized in battery systems.*

Group	Processes
Fusion Welding	Laser Beam Welding and Micro-TIG
Solid-State Welding	Friction Stir Spot Welding, Ultrasonic Welding, Magnetic Pulse Welding
Mechanical Joining	Fastening, Self-Pierce Riveting and Clinching
Plastic Deformation and Welding	Resistance Spot Welding and Resistance Projection Welding

The group of fusion welding includes processes such as laser beam welding and micro-tungsten inert gas (micro-TIG). In laser beam welding (Fig. 1.8a) the heat of fusion is provided by the energy of light beams. The beams are focused with lenses to very small surface areas, providing very high energy densities and minimizing the size of the heat-affected zone, where distortions and changes in the metallurgical structure and mechanical strength are likely to occur. The process is widely used for connecting cell terminals to busbars and for joining busbars [30].

However, because industrial lasers operate with wavelengths in the range of 0.7 μm - 1 μm (Fig. 1.9), most of the metals, apart from stainless and mild steels and, to some extent, aluminium alloys (when using a direct diode laser), are difficult to process, due to low absorption in the infrared area of the spectrum.

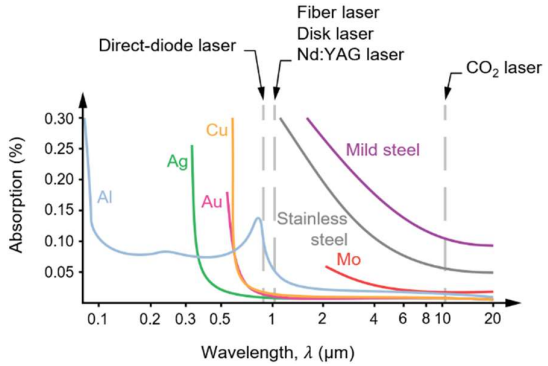

Fig. 1.9 *Absorptivity evolution with wavelength for different metals and representation of common welding laser wavelengths (adapted from [31]).*

Micro-tungsten inert gas welding is a low-cost, filler-free, welding process that uses pulsed energy source (with a typical current range of 0.5–50 A) and a non-consumable tungsten electrode to create an electric arc. The process is used to produce precision joints in stainless steels, aluminium, copper, titanium, and their alloys [32]. The pulsed energy source provides a much lower heat input than conventional TIG, but the operating parameters need to be carefully controlled to avoid excessive overheating of the battery cells when welding the cell terminals to busbar connectors. The process is used to create joints in busbars made from thin metal strips (up to 0.5 mm of thickness) and in battery cells [33].

The group of solid-state welding includes processes such as friction stir spot welding and ultrasonic welding. In friction stir spot welding (Fig. 1.8b) a rotating, threaded pin tool with a convex shaped shoulder like the one used in friction stir welding is plunged into the overlapping sheets supported by a backing plate. The shoulder ensures only partly penetration of the lower sheet by the pin tool. Friction between the tool and the two sheets heats them locally and the plastic deformation creates a solid-state bond. The process can be used in battery systems to produce joints with negligeable increase in electrical resistance when compared to those obtained by clamping [34]. However, the overall quality of the joints in hybrid busbars is very sensitive to process parameters and stability due to differences in material mixing and distribution of intermetallic compounds.

Ultrasonic welding (Fig. 1.8c) creates a metallurgical bond by simultaneous application of localized high-frequency vibratory energy and moderate normal pressures. Friction and plastic deformation at the interface deform the surface asperities and break up contaminant films and oxides resulting in direct contact between virgin surfaces and formation of a metallurgical bond. The process is used for joining cell terminals to busbar connectors in pouch-cells and has applications in a number of electric vehicles such as the Nissan Leaf, the Chevrolet Volt, the Chevrolet Spark, and the Chevrolet Bolt [29].

In magnetic-pulse welding one of the sheets is accelerated to high velocity against the other sheet placed within a small clearance. The high-energy impact and large shear strains that are developed in the two mating surfaces during the impact cause an outgoing jet of softened metal to form at the collision front that cleans the surfaces permitting subsequent solid-state bonding to occur. The process can produce high-strength joints between dissimilar materials with low heat input, eliminating the occurrence of heat-affected zones and providing high welding quality and process repeatability [35]. Magnetic-pulse welding can be used in busbar connections, namely in hybrid busbars made from thin aluminium and copper strips [36].

The group of mechanical joining includes processes such as fastening, clinching and self-pierce riveting. Fastening (Fig. 1.8d) requires drilling holes matching the diameter of the bolts (or rivets) that will be utilized to clamp the two sheets together.

This type of joints is utilized in the connection of cylindrical and prismatic cell battery terminals to busbars [37] and in busbar connections, because they are easy to assemble and disassemble during installation, maintenance and at the end of service life [38]. The Nissan Leaf and the Toyota Prius are two vehicles where this type of joints is currently used.

However, fastened joints may suffer from unintentional self-loosening caused by mechanical and/or thermal loading and from non-uniform distribution of contact resistance. The latter is caused by non-uniform distribution of pressure and roughness and makes the real contact area in overlapped busbar connections only a fraction of the nominal contact area [39]. Another limitation in the use of fasteners is related to the protrusions above and below the joints, which are not acceptable in many applications due to the increasing limitations in space of the electric power distribution systems of modern vehicles.

Self-pierce riveting is another mechanical joining process (Fig. 1.8e) that makes use of a semi-tubular (or, solid) rivet to produce a form-fit based mechanical interlock between two or more sheets. The process is generally performed at room temperature and makes use of dedicated punches and dies. The main advantage is its capability of connecting busbars made from dissimilar materials that are difficult or impossible to weld. Self-pierce riveting can be used with pre-coated sheets without damaging their surfaces and is a solution to connect busbars (and hybrid busbars) that ensures better mechanical properties under static and dynamic operating conditions than clinching [40].

Clinching is a process capable of fixing thin sheets without additional consumables or pre-drilled holes by means of dedicated punches and dies that plastically deform the sheets to achieve a form-fit based mechanical interlock. The process is generally performed at room temperature and can join monolithic or hybrid busbars as well as pre-coated busbars without damaging their surfaces. The main limitation is related to formability, which needs to be good to prevent failure by cracking. A variant of the process named as micro-clinching [41] is used in tab-to-tab connections of pouch cells.

In recent years, the authors developed two new processes with high potential of being used in the connection of monolithic and hybrid busbars. These two new processes are named as joining by double mortise-and-tenon and injection lap riveting and are shown in Fig. 1.10, in which clinching and self-pierce riveting are included for comparison purposes.

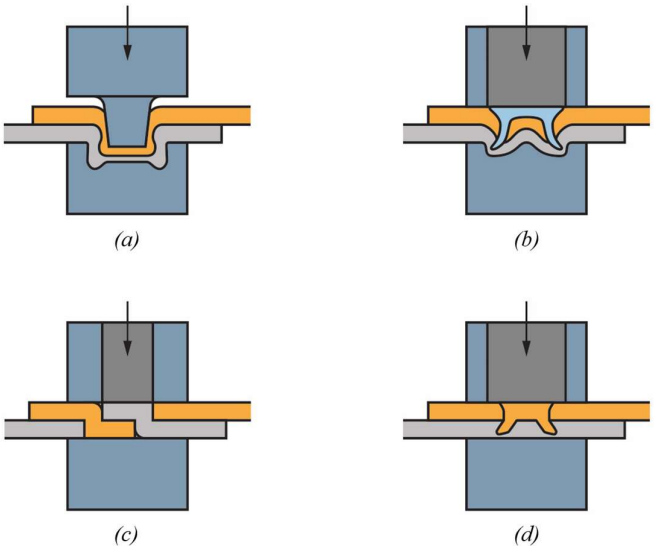

Fig. 1.10 *Mechanical joining of busbars by (a) clinching, (b) self-pierce riveting, (c) double mortise-and-tenon, and (d) injection lap riveting.*

Joining by double mortise-and-tenon (Fig. 1.10c) is built upon a combination of partial cutting and bending with form-fit joining by sheet-bulk compression of tabs in the direction perpendicular to thickness [42]. The process allows joining two overlapped busbars made from similar or dissimilar materials (e.g., copper and aluminium) and the resulting joints are flat with all the plastically deformed material contained within the thickness of the two sheets.

Injection lap riveting (Fig. 1.10d) differs from self-pierce riveting because its joining principle is based on plasticity and friction without fracture and formation of new surfaces [43]. The working principle is based on two consecutive operations - first, a dovetail ring hole is machined in the lower sheet and then a semi tubular rivet is injected through a hole in the upper sheet into the dovetail ring hole of the lower sheet, by compression with a punch. A prototype cutting tool has been proposed by the authors for producing the dovetail ring holes in-site and fostering the portability and applicability of the process.

Resistance spot welding (Fig. 1.8f) and resistance projection welding belong to a group combining plastic deformation and fusion welding. Electric current is utilized to heat the metals locally at the contacting interface. The heat softens and melt the materials locally to produce a joint. Resistance spot welding with a parallel electrode configuration is mainly used for connecting the cell terminals to busbars, but the procedure is only applicable to thin connections due to the high heat input needed to compensate the high thermal conductivities of copper and aluminium. In case of battery cells, resistance spot welding with parallel electrodes is limited to electric currents below 20 kA [26].

1.2 Analysis of busbars

The design of busbars can nowadays be made with the application of computer software based on the finite element method. Finite element modelling can easily account for the geometric and material nonlinearities as well as the real contact conditions in the joints to produce accurate predictions of electric current density, electric resistivity, temperature, stress and strain distributions, among other variables. This information is particularly relevant in case of hybrid busbars due to the utilization of materials with different thermal, electrical, and mechanical properties in joints made from sheets with different thicknesses.

This section starts by providing basic analytical design rules for hybrid busbars and ends with an overview of the theoretical fundamentals of the thermo-electrical-mechanical finite element modelling of busbars.

1.2.1 Basic analytical design of hybrid busbars

The design of hybrid busbars must account for the differences in the electric resistivity of copper and aluminium to ensure the same amount of electric current flowing though the copper and aluminium conductors of the busbars.

This is done by increasing the cross-sectional area of the aluminium according to the ratio between the electric resistivities ρ^e of the aluminium and copper. Considering, for example, a C11000 copper and an AA6000 series aluminium with $\rho^e_{Cu} = 1.68 \cdot 10^{-8}$ Ω·m and $\rho^e_{Al} = 3.80 \cdot 10^{-8}$ Ω·m, the ratio of the electric resistivities and hence the cross-sectional areas for obtaining the same conductance become,

$$A_{Al/Cu} = \frac{A_{Al}}{A_{Cu}} = \rho^e_{Al/Cu} = \frac{\rho^e_{Al}}{\rho^e_{Cu}} = 2.26 \tag{1.1}$$

Considering the mass densities of the AA6000 aluminium series and copper C11000 to be equal to $\rho_{Al} = 2680$ kg/m^3 and $\rho_{Cu} = 8900$ kg/m^3, the following

relation is obtained for the ratio $m_{Al/Cu}$ between the mass per unit length of the two conductors,

$$m_{Al/Cu} = \frac{\rho_{Al}}{\rho_{Cu}} \cdot A_{Al/Cu} = 0.68 \tag{1.2}$$

Now, considering the specific cost ratio $cost_{Al/Cu}$ of the two materials to be calculated from the specific costs 1814 €/t and 7578 €/t of the aluminium and copper, respectively, it follows that,

$$cost_{Al/Cu} = \frac{cost_{Al}}{cost_{Cu}} = 0.24 \tag{1.3}$$

and allows determining the cost ratio $€\kappa_{Al/Cu}$ of the two conductors with equal conductance as follows,

$$€\kappa_{Al/Cu} = cost_{Al/Cu} \cdot m_{Al/Cu} = 0.16 \tag{1.4}$$

The results obtained in (1.2) and (1.4) show that the utilization of aluminum when possible, reduces the mass by 32 % and the cost by 84 %, while keeping the same electric conductance. This justifies the interest of automakers in the utilization of hybrid busbars for the distribution of electric power in vehicles.

Figure 1.11 provides a schematic illustration of the cross-sectional area and weight of the copper and aluminium conductors with identical conductance. The horizontal axis shows the product of the conductance G and the length of the conductor L. With the definition $G = \frac{A}{\rho^e L}$, the slopes can be identified as stated in the figure.

Let us consider, for example, a design specification requiring a fixed value of the product between the conductance and length of the conductors $G \cdot L$. From Fig. 1.11 we can draw a vertical line to obtain the mass m and the cross-sectional area A of the copper and aluminium conductors. As seen, the results obtained confirm the utilization of hybrid busbars because although the cross-sectional area A increases when copper is replaced by aluminium, the final weight of the aluminium conductor is smaller than that of the copper conductor and the final cost of the busbar will also be smaller according to (1.4).

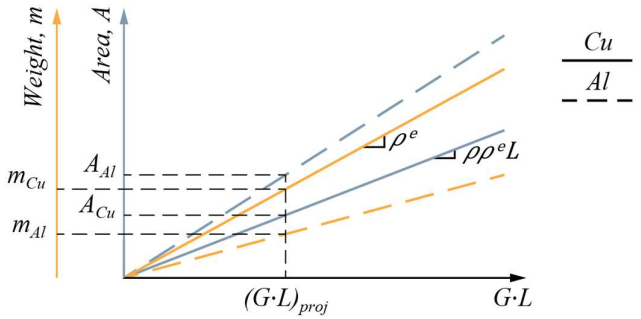

Fig. 1.11 *Graphical representation of the relations between electrical conductivity, cross-sectional area and weight for hybrid busbars made from C11000 copper and an AA6000 series aluminium.*

During this section with simple analytical calculations, the electrical connection between the copper and aluminium conductors in the hybrid busbar has been assumed ideal, i.e., without consideration of the restriction of the current flow through the connection and without considering the contact conditions in the joint. Detailed

analyses of the current flow through a joint are only possible by numerical simulations, and therefore an electro-thermo-mechanical finite element approach is presented in the following section.

1.2.2 Fundamentals of the electro-thermo-mechanical finite element analysis

The previous calculations assumed a perfect transition from copper to aluminium conductors, electric resistivities that were independent from temperature, absence of electrical and thermal resistances along the contacting surfaces due to oxides or surface roughness, among other simplifications. Electro-thermo-mechanical finite element analysis of the fabrication and operation of the busbars allows accounting for the real working conditions to optimize the performance of the busbars in service.

The finite element approach described in this section is that implemented in i-form, a finite element computer program developed by the Technical University of Denmark and the University of Lisbon [44]. The computer program is based on a strong coupling between the mechanical and thermal modules, in which the new temperature field and resulting changes in mechanical and thermal material behaviour are converged with the mechanical response including the heat generation at the end of each simulation step, and a staggered coupling with the electrical module in which the electric current density is calculated after the mechanical model to supply the thermal model with the heat generation due to Joule effect. In what follows, the fundamentals of each module are briefly introduced.

Mechanical module

The mechanical module allows modelling the deformation of the busbars and the distribution of the major field variables such as the strains and stresses, during the fabrication of the mechanical joints or the application of the required torque in the bolts and nuts of the fastened busbars. Actual contact areas between the two overlapped sheets in busbar joints can also be modelled by taking into consideration the temperature-dependent mechanical properties of the materials.

The mechanical module is built upon the finite element flow formulation, which is based on the following weak variational form of the quasi-static equilibrium equations [45],

$$\int_V \sigma_{ij}\delta\dot{\varepsilon}_{ij}\, dV - \int_{S_t} t_i\, \delta v_i dS = 0 \tag{1.8}$$

In the above equation σ_{ij} is the Cauchy stress tensor, $\dot{\varepsilon}_{ij}$ is the strain rate tensor, t_i denotes the tractions applied on the boundary S_t with a normal vector of direction cosines given by n_j, and δv_i is an arbitrary variation in the velocity because the flow formulation is written in terms of velocities.

Decomposition of the Cauchy stress tensor σ_{ij} into a deviatoric tensor $\sigma_{ij}^{'}$ related to shape changes and a hydrostatic tensor $\sigma_m = \sigma_{kk}/3$ related to volume changes, and inclusion of contact and friction between rigid and deformable objects, (e.g., between the copper and aluminium sheets of the hybrid busbar joints), allow rewriting (1.8) as follows,

$$\int_V \sigma_{ij}^{'}\delta D_{ij} dV + \int_V \sigma_m\, \delta D_v\, dV - \int_{S_t} t_i\, \delta v_i dS + \int_{S_f} \left(\int_0^{|v_r|} \tau_f \delta v_r\right) dS + K_1 \sum_{c=1}^{N_c} g_n^c \delta g_n^c = 0 \tag{1.9}$$

The symbol $D_v = \delta_{ij} D_{ij}$ is the volumetric rate of deformation and the computational approach to handle the calculation of the second term in (1.9) is done by

relaxation of the incompressibility condition of the velocity field $\sigma_m = KD_v$, where K is a large positive number known as the 'penalty' factor.

The symbols τ_f and v_r in the fourth term of (1.9) are the friction shear stress and the relative sliding velocity on the contact interfaces S_f between objects, respectively.

The fifth term accounts for the interaction between deformable bodies by means of a two-pass contact search algorithm in which the N_c contact pairs are automatically extracted from the faces of the finite elements utilized in the discretization. The symbol g_n^c stands for the normal gap velocities in the contact pairs, which is penalized by a large number K_1 to avoid penetration.

Thermal module

The thermal module calculates heat generation and transfer taking into consideration the temperature-dependent properties of the materials. The module accounts for the heat generated by plastic deformation and electrical Joule effect, and for the heat exchange between the different components of the busbars and the surrounding environment. The weak variational form of the thermal module is built upon the classical Galerkin treatment of the heat transfer equation [45],

$$\int_V kT_{,i}\delta T_{,i}\, dV + \int_V \rho\, c\, \dot{T}\delta T dV - \int_V \dot{q}_V \delta T\, dV - \int_S \dot{q}_S \delta T\, dS - \int_S kT_{,n}\, dS = 0 \qquad (1.10)$$

In the above equation, the thermal conductivity k is related to heat conduction, and the mass density ρ and the heat capacity c are related to the rate of stored energy per unit volume giving rise to a temperature gradient $\dot{T}$.

The symbol $\dot{q}_V$ in the third term of (1.10) is the rate of heat generation and includes the following contributions due to plastic deformation and Joule effect,

$$\dot{q}_{plastic} = \beta\bar{\sigma}\dot{\bar{\varepsilon}} \qquad \dot{q}_{electrical} = \rho^e j^2 \qquad (1.11)$$

where β is a factor with values in the range of 0.85 to 0.95 that gives the fraction of plastic deformation converted to heat, and ρ^e and j are the electric resistivity and the current density, respectively, used in the conversion of electric Joule effect to heat.

The symbol $\dot{q}_S$ in the fourth term of (1.10) is the rate of heat generation along surfaces and includes the following contributions,

$$\begin{aligned} \dot{q}_{convection} &= -h(T_s - T_{env}) \\ \dot{q}_{radiation} &= -\varepsilon_{emis}\sigma_{SB}(T_s^4 - T_{env}^4) \\ \dot{q}_{friction} &= \tau_f |v_r| \end{aligned} \qquad (1.12)$$

where h is the heat transfer coefficient, T_s is the surface temperature, T_{env} is the environmental temperature, σ_{SB} is the Stefan-Boltzmann constant, ε_{emis} is the emissivity number and τ_f and v_r are the friction shear stress and the relative sliding velocity on the contact interfaces between deformable and rigid objects, as previously mentioned in the mechanical module. The thermal contact conductivity is assumed ideal. This is an important aspect that will be included in future developments of the computer program [44].

The last term in (1.10) is the heat flux along the surface, where the symbol n is the vector of direction cosines of the normal to the surface.

Electrical module

The electrical module calculates the distribution of the electric potential Φ that after differentiation and multiplication by the electric conductivity provides the current density j in the busbars. The electrical module considers the temperature-dependent electrical properties of the materials, and its governing equation is built upon integration of Laplace's equation for an arbitrary variation of the electric potential $\delta\Phi$, which by applying the divergence theorem results as follows [45],

$$\int_V \Phi_{,i}\delta\Phi_{,i}dV = \int_S \Phi_{,n}dS \tag{1.13}$$

where $\Phi_{,n}$ is the normal gradient of the electric potential to the free surfaces (which is zero and therefore cancels out the right-hand side).

Although this approach considers the distribution of the electric potential Φ to be solely determined by geometry under steady conditions ($\dot{\Phi} = 0$), it is generally considered a good approximation because an electric field has a much faster reaction rate than a temperature field [44].

The current density is calculated from $j_i = \Phi_{,i}/\rho^e$, where the electrical resistivity ρ^e is temperature dependent and its value is of special importance along the contact interfaces between the two overlapped sheets of the busbar joints.

The electric contact conductivity is assumed ideal. This is another important aspect that will be included in future developments of the computer program [44].

1.3 Joining and testing of hybrid busbars

Busbars can appear in many different shapes and their joints can be fabricated by various processes belonging to the groups of fusion welding, solid-state welding, mechanical joining and plastic deformation among others that were addressed in the state-of-the-art review.

One of the determining factors for selecting joining processes is the thickness of the members to be joined. Fig. 1.12 shows an example of a resistance spot welded joint (see Fig. 1.8f) consisting of aluminium 1050A and Cu 99.5%, both of initial thickness 0.3 mm. In the specific example, a welding current of 1.53 kA was applied over a welding time of 24 ms, while the electrode force was kept at 23.2 N. The spot weld was made between tungsten electrodes with 3 mm dome radius and a flat tip diameter of 0.5 mm The resulting weld presented a typical plug failure during tensile-shear loading with a button peel out from the aluminium sheet. The tensile shear strength of a number of similar welds was around 80 N. Due to the different properties of the two sheets, there is not a weld nugget as in the case of spot welding of similar materials. Instead, the two materials bond at the interface, where small voids are observed. The cross-section in Fig. 1.12 also reveals a vertical crack (throughout the sheet thickness) in the aluminium sheet. Both voids and the vertical cracking are also observed elsewhere when spot welding aluminium in dissimilar combinations. It is, for instance, observed when joining aluminium to steel in a single-side spot welding setup [46].

Aluminium and copper are already difficult to spot weld as compared to steel due to the physical properties responsible for less heat generation and higher heat conduction away from the weld spot. Additional challenges in joining dissimilar materials are due to electrode pitting and alloying with the workpiece materials. For larger thicknesses of the sheets to be joined, the effect of heat conduction away from the weld spot increases, and the heat generation due to interface resistance also becomes relatively smaller. Therefore, spot welding is not suitable to join thicker sheets, especially in case of dissimilar materials like aluminium and copper.

When it comes to thicker sheets, mechanical joining by means of fastening and joining by forming are more appropriate solutions. The remaining part of this chapter deals with standard fastening and a recently developed joining by forming process named injection lap riveting. Material characterization and methods utilized for the fabrication and testing of the hybrid busbars of thicker sheets are presented in the following sections.

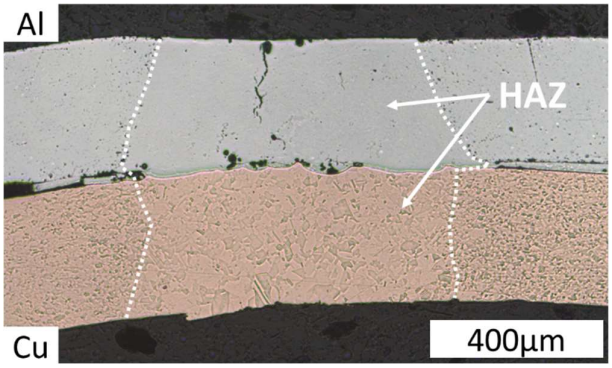

Fig. 1.12 *Cross-section of resistance spot welded aluminium 1050A to Cu 99.5% with heat affected zones (HAZ) identified by clear changes in grain sizes.*

1.3.1 Materials

The work on thicker sheets was carried out in hybrid busbar joints made from C11000 copper and AA6082-T6 aluminium sheets. Table 1.3 summarizes the electrical, thermal, and mechanical properties of the sheet materials as well as those of the medium carbon steel (class 8.8) bolts and nuts used in the fastened connections.

Table 1.3 *Summary of the electrical, thermal, and mechanical properties of the materials.*

	C11000 copper[a]	**AA6082-T6 aluminium**[a]	**Steel (class 8.8)**[a,b]
Electric resistivity (μΩ.m)	0.01845[c]	0.03935[c]	0.213
Thermal conductivity (W/(m·K))	388	170	47.7
Heat capacity (kJ/(kg·K))	0.385	0.890	0.477
Yield stress (MPa)	208.9	250	640

[a](Matweb, 2021)
[b](Bolt Depot, 2021)
[c]Experimentally determined by the authors

The true stress vs. true strain curves of the copper and aluminium sheets were obtained by means of tensile and stack compression tests and the results are shown in Fig. 1.13.

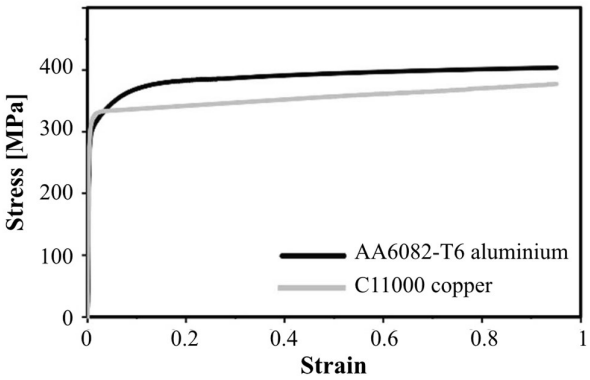

Fig. 1.13 *True-stress vs. true strain curves of the C11000 copper and the AA6082-T6 aluminium sheets.*

1.3.2 Methods and procedures

The C11000 copper and AA6082-T6 aluminium sheets utilized by the authors had 2 mm and 5 mm thickness to cope with the cross-sectional ratio $A_{Al/Cu}$ (1.4) that ensures the same conductivity values per length. The tests were performed in unit cells that are representative of the hybrid busbar joints and consisted in cutting out strips (hereafter named as sheets) with 100 mm length and 50 mm width from the copper and aluminium sheets to fabricate fastened and injected lap riveted busbar joints with 50 mm of overlap contact length (Fig. 1.14).

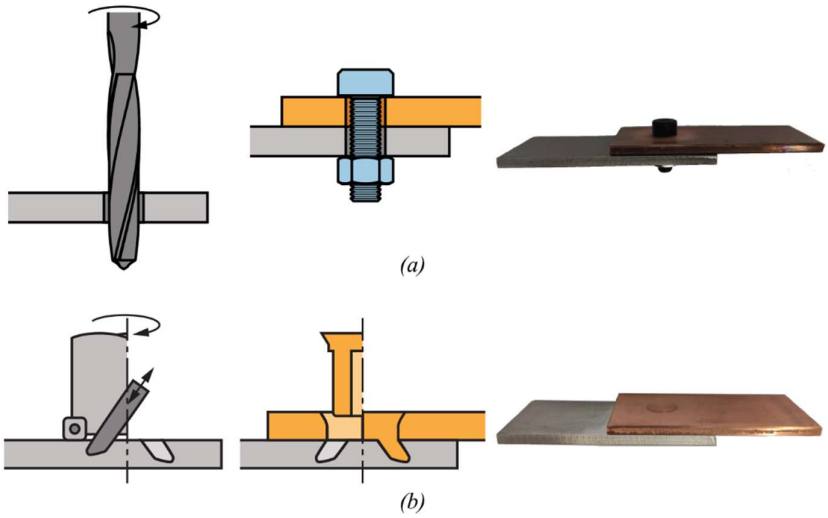

Fig. 1.14 *Schematic representation of the fabrication methods and procedures utilized to produce the (a) fastened and (b) injection lap rivet joints in hybrid busbars with photographs of the specimens.*

The fastened joints made use of M8 (class 8.8) hexagonal socket head bolts and nuts and required drilling through holes with 8.4 mm diameter in both sheets. The sheets were clamped together by applying a tightening torque of approximately 20 Nm to the bolts and nuts (Fig. 1.14a). Loosening conditions were also considered by applying smaller tightening torques.

The injection lap riveted joint required drilling countersunk holes in the copper sheets, drilling dovetail holes in the aluminium sheets with a special purpose cutter,

and machining semi-tubular rivets from C11000 copper rods with 6.6 mm of shank diameter. The rivets were injected through the copper sheets into the dovetail holes of the aluminium sheets to obtain the mechanical interlockings between the two sheets (Fig. 1.14b). Table 1.4 summarizes the fabrication conditions of both types of joints.

Table 1.4 *Fabrication conditions of the fastened and injection lap riveted joints*

<table>
<tr><td colspan="6">Fastened joints</td></tr>
<tr><td colspan="6">Medium carbon steel (class 8.8) M8 bolts and nuts</td></tr>
<tr><td>t (mm)</td><td>d (mm)</td><td>T (Nm)</td><td colspan="3" rowspan="2"> 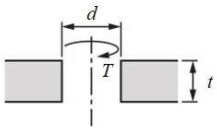

Through hole</td></tr>
<tr><td>2, 5</td><td>8.4</td><td>20</td></tr>
<tr><td colspan="6">Injection lap riveted joints</td></tr>
<tr><td colspan="6">C11000 copper sheets</td></tr>
<tr><td>t (mm)</td><td>α (º)</td><td>d (mm)</td><td>p (mm)</td><td colspan="2" rowspan="2"> 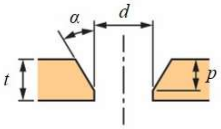

Countersunk hole</td></tr>
<tr><td>2</td><td>45</td><td>7.3</td><td>1.5</td></tr>
<tr><td colspan="6">AA6082-T6 aluminium sheets</td></tr>
<tr><td>t (mm)</td><td>α (º)</td><td>p (mm)</td><td>h (mm)</td><td colspan="2" rowspan="2"> 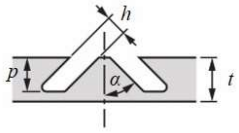

Dovetail ring hole</td></tr>
<tr><td>5</td><td>30</td><td>4</td><td>2.3±0.1</td></tr>
<tr><td colspan="6">C11000 copper semi-tubular rivets</td></tr>
<tr><td>d_i (mm)</td><td>d_o (mm)</td><td>D (mm)</td><td>H (mm)</td><td>s (mm)</td><td rowspan="2"> 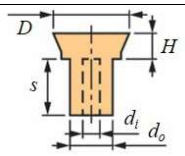
</td></tr>
<tr><td>2.0±0.1</td><td>6.6±0.1</td><td>10</td><td>2.2</td><td>6.9</td></tr>
</table>

The unit cells containing the hybrid busbar joints were placed in a test setup for measuring the electrical resistance under laboratory-controlled conditions. The setup is shown in Fig. 1.15 and consists of two copper-blocks, where the busbar ends are clamped and connected to the power supply of a micro-ohmmeter. A current of 600 A is passed through the busbars during approximately 5 s to allow measuring the induced voltage V and the electrical resistance by means of two probes applied at the busbar ends.

Because the temperature does not change significantly during the 5 s duration of the tests, it is assumed that the measured values of electric resistance remain constant during the entire duration of each test.

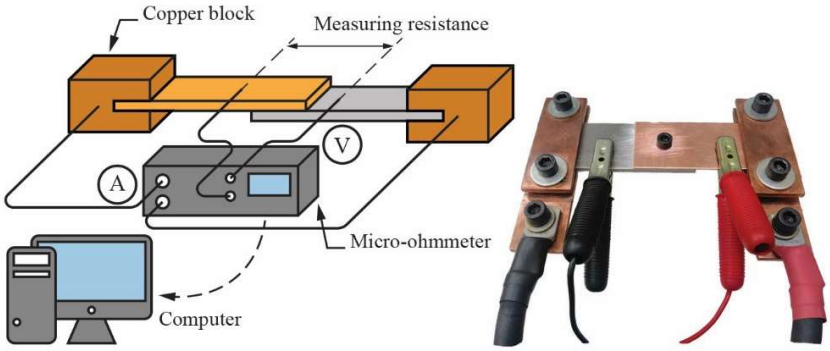

Fig. 1.15 *Schematic representation of the testing setup used for measuring the electrical resistance of the hybrid busbar joints with photograph. The distance between the measuring probes is 100 mm and was kept identical in all the tests.*

1.4 Results, discussion, and future perspectives

1.4.1 Injection lap riveting of the hybrid busbar joints

Although the hybrid busbars are not axisymmetric, their mechanical joining by means of injection lap riveting involves plastic deformation in a limited amount of volume located around the dovetail ring hole (Fig. 1.16). This justifies the reason why finite element analysis can be performed under axisymmetric modelling conditions and why the meshes of the copper and aluminium sheets can be designed to account only for the material located around the dovetail ring holes where the rivets are to be inserted [43].

The working principle of injection lap riveting is easily inferred from the initial and final meshes shown in Fig. 1.16a. As seen, the copper sheet acts as an injection chamber and the pre-drilled dovetail ring hole behaves as a die cavity into which the shank length of the semi-tubular rivet is injected by compression with a punch. No material protrusions are left above and below the surfaces at the end of the joining process because the deformed rivet is accommodated inside the two sheets.

The evolution of the riveting force with punch stroke is made of three main zones corresponding to different penetration depths of the semi-tubular rivets inside the dovetail ring holes. The first zone (labelled as ‘A’) corresponds to the contact with sliding of the inner semi-tubular rivet wall along the inner surface of the dovetail ring hole. The second zone (labelled as ‘B’) starts when the outer semi-tubular rivet wall starts contacting and sliding along the outer surface of the dovetail ring hole. The third zone (labelled as ‘C’) corresponds to the contact of the rivet head against the countersunk surface hole of the copper sheet.

The overall agreement between the experimental and the numerically predicted riveting forces is very good and proves the effectiveness of i-form in simulating the mechanical joining of busbars.

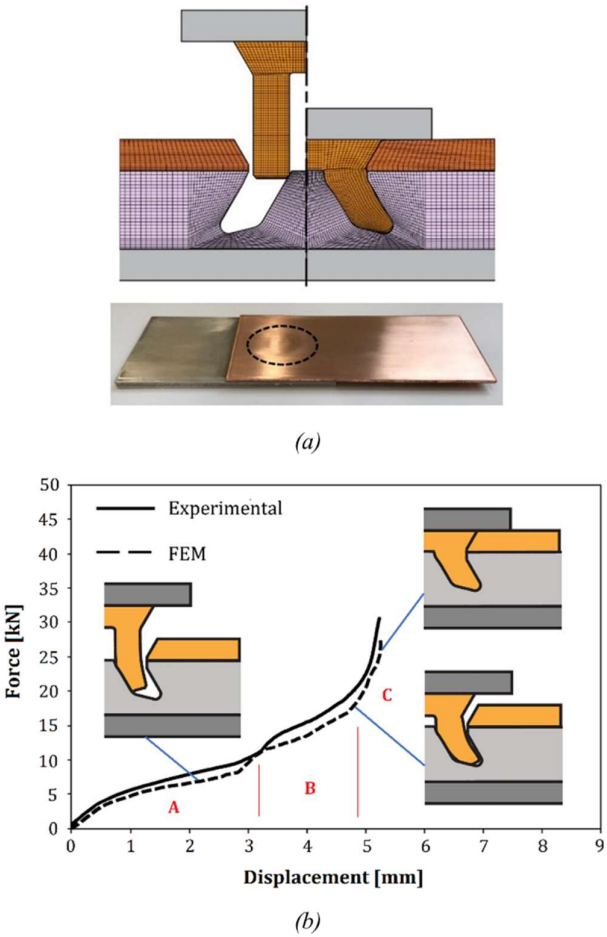

Fig. 1.16 *Fabrication of a hybrid busbar joint by injection lap riveting. (a) Initial and final predicted finite element cross-sections of the joint with photograph and (b) experimental and finite element predicted evolution of the riveting force with the punch stroke.*

1.4.2 Hybrid busbar joints in service

The numerical simulation of the electric current flowing through the hybrid busbars produced by fastening and injection lap riveting cannot be done under 2D axisymmetric modelling conditions because electric current flows through the entire busbar length. Full three-dimensional models like those shown in Fig. 1.17 are required.

The finite element predicted distribution of current density j for the hybrid busbar joints produced by fastening and injection lap riveting assumed ideal preparation of the sheet surfaces before joining and measuring to avoid results being influenced by the presence of copper and aluminium oxide films. As seen, the current density j is higher in the copper sheet ($j_{Cu} = 6.0$ A/m^2) than in the aluminium sheet ($j_{Al} = 2.4$ A/m^2), and the ratio $j_{Al}/j_{Cu} = 2.5$ matches the ratio $A_{Al}/A_{Cu} = 2.5$ to ensure a near constant electric current flow through the busbar (refer also to equation (1.4)).

The finite element predicted distribution of current density shows that the new semi-tubular rivet produces a smaller electrical disruption than the fastened joint consisting of a bolt with a nut. As a result of this, the computed equivalent resistance in the 100 mm distance marked in Fig. 1.17 is smaller (15.6 μΩ vs15.8 μΩ). These values are smaller than the experimental values measured with the probes in the testing apparatus of Fig. 1.15 (18.9 μΩ vs 17.5 μΩ) because the contact conditions

between the overlapped sheets were not ideal both from a chemical and a mechanical point of view. In case of the later, it was possible to observe contactless areas along the sheet edges of overlapped region.

Still, the results obtained by the authors confirm the advantages of using the new type of joints in real applications comprising long busbars with several connections. The absence of protrusions above and below the sheet surfaces and the overall stability of the connection, which is not sensitive to the loosening effects of fastened joints that provided resistance values an order of magnitude above (e.g., 150 μΩ) when the bolts and nuts were tightened by hand, further confirm the advantages of the new proposed joints.

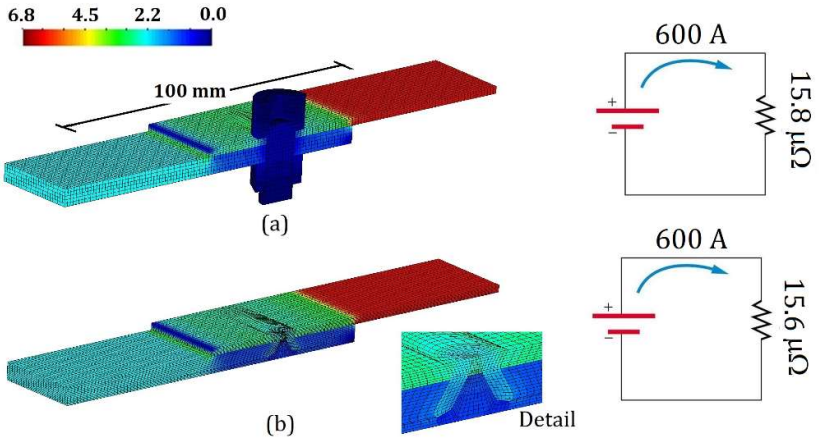

Fig. 1.17 *Finite element distribution of current density (A/mm2) for hybrid busbars joints produced by (a) fastening and (b) by injection lap riveting with indication of the distance between the measuring probes and the numerically predicted values of electric resistance.*

1.4.3 A new portable cutting tool concept

The dovetail ring holes utilized in the hybrid busbars were fabricated by turning using a special purpose cutter. Ongoing developments by the authors comprise the development of a portable cutting tool concept that is schematically illustrated in Fig. 1.18 to foster the applicability of the new proposed injection lap riveting process in-site [24, 43].

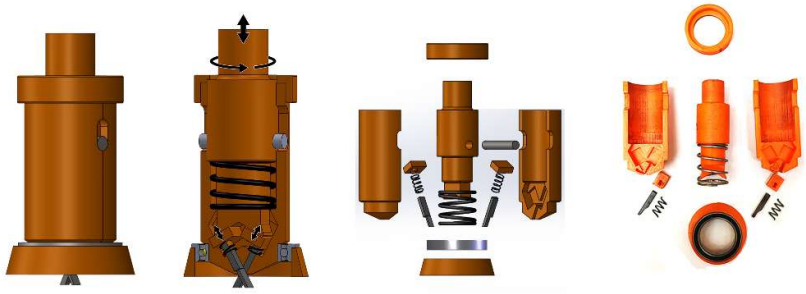

Fig. 1.18 *The portable cutting tool concept for drilling dovetail ring holes in sheets and the corresponding additive manufacturing prototype.*

The tool consists of two inclined cutters controlled by springs that will progressively open to deepen the dovetail holes as the upper table moves down. The tool can be easily attached to a drilling machine and used as a portable milling machine.

The design of the tool is flexible and allows easy and fast replacement of the inclined cutters for sharpening. A prototype of the cutting tool was fabricated by additive manufacturing using a fused filament fabrication (FFF) machine and dovetail ring holes were successfully fabricated in wood and polymer testing materials. The tool is now being redesigned to allow machining the dovetail ring holes in metal sheets.

1.5 Conclusions

Electric mobility is keeping the forming industry on their toes due to opportunities in the production of components for asynchronous motors, lightweight body-in-white structures, and busbar systems for the distribution of electric power. Hybrid busbars made from copper and aluminium combine the electric resistivity advantages of copper with the lightweight and economic advantages of aluminium in such a way that the thinner and costlier parts made from copper are only used in specific key locations.

The use of aluminium in hybrid busbars comes at a cost of diminishing the current carrying capacity, increasing the overall impedance of busbars, and creating technical difficulties in joining with copper. Results show that although the cross section of aluminium must be 2.3 times greater than that of copper to ensure a similar conductance, savings in weight and cost resulting from the use of hybrid busbars are approximately equal to 32% and 76%, respectively.

The growing interest of automakers in the use of hybrid busbars stimulated the authors to develop a new injection lap riveting process to produce overlap joints by plastic deformation of a semi-tubular rivet made from the softer material. The process is carried out in two stages, in which a dovetail ring hole is first machined in the harder sheet and a semi-tubular rivet is then injected through the softer sheet into the dovetail hole of the harder sheet to obtain a mechanical interlocking.

Laboratory measurements of electric resistance in hybrid busbars produced by injection lap riveting and comparison with the values obtained in conventional fastened solutions demonstrate the effectiveness of the new joining by forming concept. An electro-thermo-mechanical finite element computer program developed by the authors also reveals its effectiveness for the analysis of busbars due to its dual capability of modelling the joining by forming process and the behavior of the busbars under the application of an electric current.

Acknowledgments

The authors would like to acknowledge the support provided by Fundação para a Ciência e a Tecnologia and IDMEC under LAETA-UID/EMS/50022/2013 and PTDC/EME-EME/0949/2020. The work of MSc. Francisco Ferreira is also acknowledged.

References

[1] Grauers A, Sarasini S, Karlström M (2017) Why electromobility and what is it. In: (Ed. Sandén B, Wallgren P) Systems Perspectives on Electromobility. Chalmers University of Technology, Gothenburg.

[2] Barbier EB (2020) Building a greener recovery: lessons from the great recession. United Nations Environment Programme, Geneva.

[3] Santos DMF, Sequeira CAC, Figueiredo JL (2013) Hydrogen production by alkaline water electrolysis, Química Nova, 36, 1176–1193. doi:10.1590/S0100-40422013000800017.

[4] Ursúa A, Gandía LM, Sanchis P (2012) Hydrogen Production from Water Electrolysis: Current Status and Future Trends, Proceedings of the IEEE, 100(2), 410–426.
[5] Agrawal KC (2007) Carrying power through metal-enclosed bus systems. In: Electrical power engineering reference and applications handbook. CRC Press, Boca Raton.
[6] Siemens AG (2013) Gas-insulated switchgear up to 550 KV, 63 KA, 5000 A type 8DQ1, Erlangen. https://www.siemens-energy.com/global/en/offerings/power-transmission/transmission-products/gas-insulated.html, accessed on Feb 11, 2021.
[7] Chapman D, Norris T (2014) Copper for Busbars: Guidance for Design and Installation. Copper Development Association, Hemel Hempstead.
[8] Kim M-J, Bak S-H, Jung W-C, Hur D-J, Ko D-S, Kong M-S (2019) Improvement of Heat Dissipation Characteristics of Cu Bus-Bar in the Switchboards through Shape Modification and Surface Treatment, Energies 12(1), 146. doi:10.3390/en12010146.
[9] Dion PA (1968) Metal cladding, US3616982A, United States Patent.
[10] Jehyeon B (1996) Method for Manufacturing Bus-Bar, Korean Patent KR970004548B1.
[11] Davis JR (Ed.) (2001) ASM Specialty Handbook – Copper and Copper Alloys. ASM International, Materials Park, OH.
[12] ASM International (1990) ASM Handbook Volume 2: Properties and Selection: Nonferrous Alloys and Special-Purpose Materials. ASM International, Materials Park, Ohio.
[13] Groover MP (2010) Fundamentals of Modern Manufacturing: Materials, Processes, and Systems. John Wiley & Sons, Hoboken, NJ.
[14] Melsom SW, Booth HC (1922) The Efficiency of Overlapping Joints in Copper and Aluminium Busbar Conductors, Journal of the Institution of Electrical Engineers, 60, 312, 889–899 (1922). doi:10.1049/jiee-1.1922.0068.
[15] Iclodean C, Varga B, Burnete N, Cimerdean D, Jurchiș B (2017), Comparison of Different Battery Types for Electric Vehicles, CAR2017 International Congress of Automotive Transport Engineering - Mobility Engineering and Environment, 252.
[16] Zwicker MFR, Moghadam M, Zhang W, Nielsen CV (2020) Automotive battery pack manufacturing – a review of battery to tab joining, Journal of Advanced Joining Processes, 1, 100017. doi: 10.1016/j.jajp.2020.100017.
[17] Gallagher KG, Nelson PA (2014) Manufacturing costs of batteries for electric vehicles. In: (Ed. Pistoia G) Lithium-Ion Batteries: Advances and Applications. Elsevier: Amsterdam.
[18] Accelonix (2021) Introduction to wire bonding in production of battery packs. https://accelonix.co.uk/index.php/microelectronics/fully-automatic-wire-bonder/wire-bonding-in-production-of-battery-packs, accessed on May 12, 2021.
[19] Gabzdyl J, Dzurko K, SPI Lasers UK LTD (2019) E-mobility offers multiple opportunities for fiber lasers. https://www.spilasers.com/case-study-e-mobility/e-mobility-offers-multiple-opportunities-for-fiber-lasers/, accessed on May 12, 2021.
[20] AUDI AG (2021) Audi e-tron Sportback 55 quattro. https://www.audi-mediacenter.com/en/search?query=batterie%20etron&type=image&utf8=%E2%9C%93, accessed on May 12, 2021.
[21] EV battery center (2014) 2kWh Lithium Battery Pack Chevrolet Volt – 47V/47Ah/12 cells. https://evbatterycenter.com/HAC4/index.php?option=com_hikashop&ctrl=product&task=show&cid=79&name=2kw-h-lithium-battery-pack-chevrolet-volt-45v-45ah-12-cells&Itemid=605, accessed on May 12, 2021.
[22] Second life EV batteries Ltd (2021) BMW i3 |44V | 94Ah. https://www.secondlife-evbatteries.com/products/bmw-i3-module-samsung-sdi-94ah, accessed on May 12, 2021.
[23] Saariluoma H, Piiroinen A, Unt A, Hakanen J, Rautava T, Salminen A (2020) Overview of Optical Digital Measuring Challenges and Technologies in Laser Welded Components in EV Battery Module Design and Manufacturing, Batteries, 6, 47. doi:10.3390/batteries6030047.
[24] Ferreira F (2020) Dissimilar metal joining through injection riveting, MSc. Dissertation, Instituto Superior Técnico, University of Lisbon.
[25] Porsche AG (2019) The Porsche Taycan. https://e-performance.io/en/taycan-technology, accessed on Feb 20, 2021.
[26] Brand MJ, Philipp AS, Michael FZ, and Andreas J (2015) Welding techniques for battery cells and resulting electrical contact resistances, Journal of Energy Storage, 1, 7-14. doi:10.1016/j.est.2015.04.001.
[27] Fleckenstein M, Bohlen O, Roscher MA, Bäker B (2011) Current density and state of charge inhomogeneities in Li-ion battery cells with LiFePO4as cathode material due to temperature gradients, Journal of Power Sources, 196 (10), 4769–4778. doi:10.1016/j.jpowsour.2011.01.043.
[28] Kaspar J, Zimmermann M, Ostwaldt A, Goebel G, Standfuß J, Brenner B (2014) Challenges in joining aluminium with copper for applications in electro mobility, Materials Science Forum, 783–786, 1747–1752. doi:10.4028/www.scientific.net/msf.783-786.1747.
[29] Das A, Li D, Williams D, Greenwood D (2018) Joining Technologies for Automotive Battery Manufacturing, World Electric Vehicle Journal, 9. doi:10.3390/wevj9020022.
[30] Katayama S (2013) Introduction: fundamentals of laser welding. In: (Ed. Katayama S) Handbook of laser welding technologies. Woodhead Publishing, Cambridge.

[31] Mahamood RM (2017) Laser Basics and Laser Material Interactions. In: (Ed. Mahamood RM) Laser Metal Deposition Process of Metals, Alloys, and Composite Materials. Springer, Cham, doi: 10.1007/978-3-319-64985-6_2.

[32] Wang J, Katsumoto K, Nezu K (2004) Investigation into micro-tungsten inert gas arc behaviour and weld formation, Science and Technology of Welding and Joining, 9, 1, 90–94. doi: 10.1179/136217104225017198.

[33] Alexy M, van de Wall D, Shannon G, Boyle ML (2019) Batteries need strong connections – are resistance, laser and micro TIG welding the best suited joining technologies?, Biuletyn Instytutu Spawalnictwa, 1, 53–63. doi:10.17729/ebis.2019.1/6.

[34] Oláfsson D, Vilaça P, Vesanko J (2020) Multiphysical characterization of FSW of aluminum electrical busbars with copper ends, Welding in the World, 64, 59–71. doi:10.1007/s40194-019-00814-0.

[35] Wu X, Shang J (2014) An Investigation of Magnetic Pulse Welding of Al/Cu and Interface Characterization, Journal of Manufacturing Science and Engineering, 136, 5. doi:10.1115/1.4027917.

[36] PST Products (2019) EMPT in the battery production. https://www.pstproducts.com/en/empt_battery_production.html, accessed on Feb 15, 2021.

[37] Lee SS, Kim TH, Hu SJ, Cai W (2010) Joining Technologies for Automotive Lithium-Ion Battery Manufacturing: A Review, ASME 2010 International Manufacturing Science and Engineering Conference, 541–549.

[38] Agrawal KC (2007) Recommended Practices for Mounting Buses and Making Bus Joints. In: Electrical power engineering reference and applications handbook. CRC Press, Boca Raton.

[39] Tzeneva R, Slavtchev Y, Mladenov V (2007) New connection design of high power bolted busbar connections, Proceedings of the 11th Conference on Proceedings of the 11th WSEAS International Conference on Circuits - Volume 11 (ICC'07), 228–233.

[40] Xing B, He X, Wang Y, Yang H, Deng C (2015) Study of mechanical properties for copper alloy H62 sheets joined by self-piercing riveting and clinching, Journal of Materials Processing Technology, 216, 28–36. doi:10.1016/j.jmatprotec.2014.08.030.

[41] Wang X, Li C, Ma Y, Shen Z, Sun X, Sha C, Gao S, Li L, Liu H (2016) An Experimental Study on Micro Clinching of Metal Foils with Cutting by Laser Shock Forming, Materials 9, 7. doi:10.3390/ma9070571.

[42] Pragana JPM, Silva CMA, Bragança IMF, Alves LM, Martins PAF (2018) A new joining by forming process to produce lap joints in metal sheets, CIRP Annals, 67, 1, 301–304. doi:10.1016/j.cirp.2018.04.121.

[43] Ferreira FR, Pragana JPM, Bragança IMF, Silva CMA, Martins PAF (2021) Injection lap riveting, CIRP Annals Manufacturing Technology (accepted for publication). doi: 10.1016/j.cirp.2021.03.018

[44] Nielsen CV, Zhang W, Alves LM, Bay N, Martins PAF (2013) Coupled finite element flow formulation In (Ed. Davim P): Modelling of thermo-electro-mechanical manufacturing processes with applications in metal forming and resistance welding, Springer-Verlag, London, (doi: 10.1007/978-1-4471-4643-8_3)

[45] Nielsen CV, Martins PAF (2021) Finite element flow formulation In: Metal forming: formability, simulation and tool design, Academic Press, London. (https://doi.org/10.1016/B978-0-323-85255-5.00008-X)

[46] Szallies K, Zwicker M, Bergmann JP (2020): Single-sided resistance spot welding of steel-aluminum dissimilar joints - Mechanical characterization and interface formation. Advanced Structured Materials 125. doi: 10.1007/978-981-15-2957-3_6